Plug-and-play nucleic acid-mediated multimerization of biparatopic nanobodies for molecular imaging

Laura Teodori,[1] Sarah K. Ochoa,[1] Marjan Omer,[1] Veronica L. Andersen,[1] Pernille Bech,[1] Junyi Su,[1] Jessica Bridoux,[2] Jesper S. Nielsen,[1] Mathias B. Bertelsen,[1,3] Sophie Hernot,[2] Kurt V. Gothelf,[1,3] and Jørgen Kjems[1,4]

[1]Interdisciplinary Nanoscience Center (iNANO), Aarhus University, Gustav Wieds Vej 14, 8000 Aarhus C, Denmark; [2]Molecular Imaging and Therapy Laboratory (MITH), Vrije Universiteit Brussel (VUB), Building K, Laarbeeklaan 103, 1090 Brussels, Belgium; [3]Department of Chemistry, Aarhus University, Langelandsgade 140, 8000 Aarhus C, Denmark; [4]Department of Molecular Biology and Genetics, Universitetsbyen 81, 8000 Aarhus C, Denmark

In cancer molecular imaging, selecting binders with high specificity and affinity for biomarkers is paramount for achieving high-contrast imaging within clinical time frames. Nanobodies have emerged as potent candidates, surpassing antibodies in pre-clinical imaging due to their convenient production, rapid renal clearance, and deeper tissue penetration. Multimerization of nanobodies is a popular strategy to enhance their affinity and pharmacokinetics; however, traditional methods are laborious and may yield heterogeneous products. In this study, we employ a Holliday junction (HJ)-like nucleic acid-based scaffold to create homogeneous nanostructures with precise multivalent and multiparatopic nanobody displays. The plug-and-play assembly allowed the screening of several nanobody multimer configurations for the detection of the breast cancer biomarker, human epidermal growth factor receptor 2 (HER2). *In vitro* studies demonstrated significant improvements in binding avidity, particularly with the biparatopic construct exhibiting high sensitivity, surpassing that of traditional antibody-based cell binding. Furthermore, our HJ platform allowed for adaptation from fluorescence-based to nuclear imaging, as demonstrated in xenografted mice, thereby allowing for future *in vivo* applications. This work highlights the potential of nucleic acid-mediated multimerization to markedly enhance nanobody binding, by exploring synergistic combinations and offering versatility for both *in vitro* diagnostics and cancer molecular imaging with prospects for future theranostic applications.

INTRODUCTION

Molecular imaging relies on the visualization of specific biomarkers and can provide both qualitative and quantitative information about the molecular mechanisms characterizing a pathology. Its advancements in oncology have improved patient prognoses through more precise diagnosis and evaluation of the developmental stage and aggressiveness of the disease. In addition, molecular imaging has enabled tailored therapies and facilitated the assessments of treatment response.[1,2] To provide high-contrast images of cancerous tissues, targeted imaging probes require highly stable and clinically safe targeting ligands. These should bind with high affinity and specificity to the biomarker and hence accumulate in sufficiently high concentration in the tumors, while rapidly clearing from non-target tissues.[3,4] One example of such ligands is monoclonal antibodies (mAbs) that can bind with nanomolar affinity to cancer-specific biomarkers[5] and have offered interesting targeting strategies for immunotherapy[6,7] and molecular imaging. Particularly, antibody-based tracers can be used to assess the pharmacokinetics and biodistribution before administering a corresponding antibody-based therapy.[8,9] However, owing to their large size (~150 kDa),[9] mAbs exhibit long circulation times and poor tissue penetration leading to heterogeneous accumulation in tumors. Hence, high-contrast images obtained by mAbs labeled with long-lived radionuclides can only be imaged hours or days from the time of administration.[7,10] To address the effects of the large size of mAbs and their costly production, smaller antibody fragments were developed. The most prominent antibody fragments are camelid-derived single-domain antibody fragments, also known as nanobodies (Nbs). Nbs present an attractive alternative for applications in diagnostics and therapy[11] and have potential as tracers for high-contrast imaging of tumors in molecular imaging.[12] They can be selected to bind virtually any desired antigen while allowing easy sequence engineering, lower immunogenicity, and inexpensive production in bacteria and yeast.[13,14] Nbs are readily labeled with fluorophores or radionuclides for optical or nuclear imaging, either randomly[15] or site specifically, through, i.e., engineered cysteines,[16,17] sortase A tags,[18,19] or functionalized unnatural amino acids.[20] Their small size (~15 kDa) enables deeper tissue penetration and rapid renal clearance, enhancing the signal-to-noise ratio by rapidly eliminating circulating Nbs.[21,22] This substantially reduces acquisition time and minimizes exposure to the radiolabeled Nbs.[7] However, their fast circulation time rapidly diminishes their local optimal

concentration, thereby limiting the potential for achieving an optimal site-specific accumulation.[23] To tackle this issue, multimerization strategies can be used to offer notable advantages for Nb applications in molecular imaging. Firstly, the binding affinity is improved through avidity.[24,25] Secondly, the circulation half-life of the tracer can be adjusted by varying the Nb valence,[26] allowing for optimization of the tracer's bioavailability to enhance imaging. This approach demands the rational design of Nb multimers to fulfill dual criteria: an improved tracer retention specifically located in the targeted tissue and an optimal circulation time ensuring sufficient accumulation at the target site and rapid blood clearance, thus increasing the signal-to-noise ratio of the resulting image.[27]

Multimerized identical or non-identical Nbs can be created via genetic fusion[28] or by multivalent display on particles such as micelles,[29] gold nanoparticles,[30] and lipid-coated nano-[31] and microbubbles,[32] yielding compact multivalent (binding the same epitope), multiparatopic (binding different epitopes on the same antigen), or multispecific (binding different antigens) Nb-based agents.[33–35] Even though protein engineering techniques allow for the production of these well-defined multimer combinations, there are still challenges to be addressed as this process is often laborious and yields insufficient product homogeneity and quantities that are not relevant for clinical use.[36]

In this study, the 2Rs15d and 2Rb17c Nbs,[37] targeting two different epitopes of the human epidermal growth factor receptor 2 (HER2),[38] were multimerized into homogeneously configured homobivalent and biparatopic nanostructures (anti-HER2 HJs) to increase the avidity of the Nbs toward their target and improve HER2 detection. As a multimerization scaffold, we chose the non-immunogenic, highly thermostable, and nuclease-resistant nucleic acid-based Holliday junction (HJ) composed of $2'$-O-methyl- and LNA-modified nucleotides.[39,40] The helical stacking of the six-base-paired arms in the four-module configuration confers improved thermal stability *in vivo*.[39,40] The HJ scaffold also offers a stoichiometrically controlled plug-and-play assembly of synergistic combinations of the two Nbs, enabling the fast and efficient affinity screening of multiple constructs *in vitro* and *in vivo*. This work provides insight into the effect of homologous and heterologous multimerization of Nbs on their combined avidity toward the HER2 receptor and highlights the advantages and pitfalls of employing a nucleic acid-based scaffold for multimerization purposes.

RESULTS

Functionalization and characterization of the anti-HER2-HJ nanostructures

To multimerize the Nbs, we used the chemically modified HJ nanoscaffold consisting of the four oligonucleotide modules Q1, Q2, Q3, and Q4 (Figure 1A).[39] The anti-HER2 Nbs, 2Rs15d and 2Rb17c, and the non-targeting control R3B23 Nb (binding the 5T2MM M-protein in multiple myeloma tumors)[41] were recombinantly expressed with a C-terminal azido (N_3) group in *E. coli*, as described previously.[20] The azido-modified Nbs were reacted with dibenzocyclooctyne (DBCO)-labeled Q1 and Q4 modules in a strain-promoted

alkyne-azide cycloaddition (SPAAC) reaction to obtain the bioconjugates Q1-Nb and Q4-Nb (Figures 1B and 1C).

Combining equimolar amounts of Q-Nb bioconjugates and unconjugated Q-modules to self-assemble into the HER2-targeting (anti-HER2) or non-targeting (negative control) HJ constructs yielded monovalent, homobivalent, and biparatopic display of Nbs (schematics in Figure 1A). The annealing of the HJs successfully reached complete conversion into fully assembled constructs (Figure 1D), circumventing their purification from unassembled modules.

The *in vitro* screening included eight different HJ constructs. Monovalent HJ-1x2Rs15d and HJ-1x2Rb17c bearing only one of the two anti-HER2 Nbs, homobivalent HJ-2x2Rs15d and HJ-2x2Rb17c bearing two copies of the same Nb, and biparatopic HJ-2Rs15d-2Rb17c bearing two different anti-HER2 Nbs, and negative control constructs represented either by a naked HJ (displaying no Nbs, denoted as "HJ" in Figure 1A), a monovalent HJ-1xR3B23, or a homobivalent HJ-2xR3B23, both bearing the non-targeting R3B23 Nb.

Binding of anti-HER2 HJ constructs

The binding activity of the anti-HER2 HJs to their target was tested by bio-layer interferometry (BLI), where recombinant HER2 dimer-Fc chimeras were immobilized on anti-human IgG-functionalized biosensors and subjected to the various HJ constructs in solution.

The association and dissociation profiles of the monovalent anti-HER2 HJs showed a clear difference in the binding kinetics of the two conjugated Nbs, which is in agreement with the kinetic studies of the free 2Rs15d and 2Rb17c Nbs reported by D'Huyvetter et al.[38] and Debie et al.[22] (Figures 2A and 2B). Compared with HJ-1x2Rs15d, HJ-1x2Rb17c exhibited a more rapid association, followed by a faster dissociation rate, as confirmed by the k_{on} and k_{off} values reported in the table in Figure 2H. Nevertheless, the K_D values of both monovalent constructs were maintained at low nM values and are comparable with K_D values reported for the unmodified[37] and the N_3-modified Nbs.[20] This confirms that the conjugation and assembly into HJs did not affect the binding kinetics of the Nbs.

The homobivalent constructs, HJ-2x2Rb17c and HJ-2x2Rs15d showed a highly improved binding to HER2 as indicated by the increase in response (shift in nm) and an overall faster association compared with the monovalent counterpart (Figures 2C and 2D). The Nb-specific binding kinetics were maintained, ranking the HJ-2x2Rb17c as the fastest binder among all tested constructs. Moreover, both constructs exhibited greater binding stability during the dissociation phase compared with the monovalent nanostructures, as confirmed by a decrease in k_{off} of 4.3- and 17.6-fold for the HJ-2x2Rs15d and HJ-2x2Rb17c, respectively (Figure 2H), which resulted in a decrease of K_D values to very low nanomolar ranges for both homobivalent constructs.

Finally, the biparatopic HJ-2Rs15d-2Rb17c exhibited the highest response (Figure 2E), indicating a larger increase in the number of
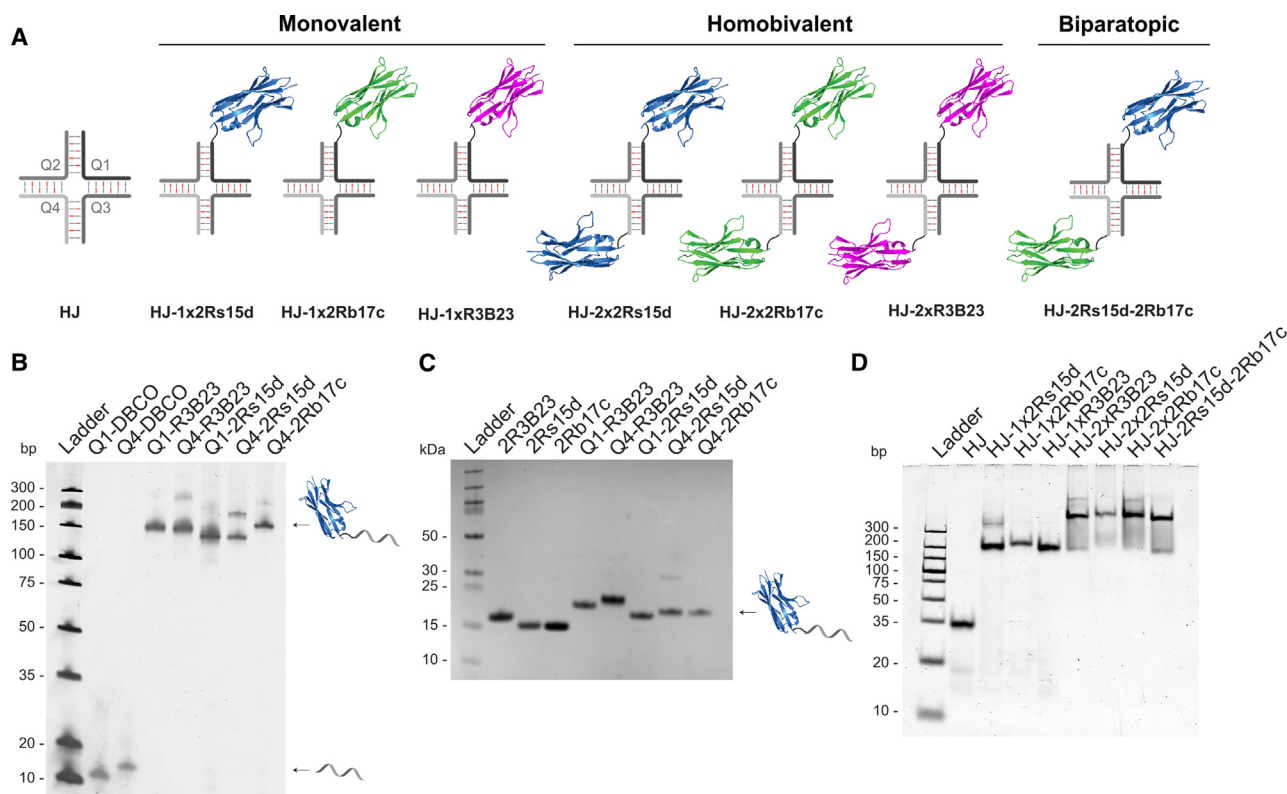
Figure 1. HJ functionalization with anti-HER2 Nbs
(A) Schematics of the various HJ constructs displaying none, mono- or homobivalent, or biparatopic configurations of the Nbs indicated below. The HJ scaffold consists of four oligonucleotides (Q1-4) constituted by LNA (red) and 2′-OMe (gray) nucleotides. (B) Urea PAGE gel (12%) displaying DBCO-functionalized Q1 and Q4 and the Nb-oligonucleotide bioconjugates after purification. (C) SDS-PAGE gel displaying the free Nb-N_3 and the Nb-oligonucleotide bioconjugates. (D) Native PAGE gel (12%) displaying HJ constructs bearing anti-HER2 or negative control Nbs in different configurations.

bound HJs with respect to all the other anti-HER2-HJ constructs. While the association rate was comparable with that observed for the HJ-2x2Rs15d, the dissociation rate appeared as the slowest, indicating stronger binding stability compared with the homobivalent constructs. This was confirmed by its k_{off} value, which was the lowest observed among all the anti-HER2 HJ constructs. As anticipated, no detectable signal was observed for the negative control constructs, the naked HJ, and the HJ-2xR3B23 (Figures 2F and 2G).

Targeting activity of anti-HER2 HJs toward HER2-expressing cancer cell line
The HER2 receptor is expressed at different levels in different types of tumors. To assess the binding activity and specificity of the anti-HER2 HJs to cancer cells, we tested three human breast cancer cell lines expressing the HER2 receptor to different degrees, SkBr3 (HER2+++), MCF-7 (HER2+), and MDA-MB-231 (HER2−), by flow cytometry. To enable detection, a Cy5-labeled Q2 module was included in the anti-HER2 and negative control HJs (Figure S1).

Flow cytometry showed HER2-dependent binding of all anti-HER2 HJs to the three cell lines (Figure 3A). In accordance with reported expression levels,[42–44] the SkBr3 cells showed the strongest binding

for all the constructs, followed by medium-to-low binding to MCF-7 and low-to-no binding to the MDA-MB-231 cells. As anticipated, the naked HJ and non-targeting HJ-2xR3B23 showed no detectable binding across all three cell lines.

Conforming with the binding stability measured by BLI, monovalent HJ-1x2Rs15d exhibited a higher binding signal than monovalent HJ-1x2Rb17c (7-fold for SkBr3 cells). The homobivalent display of both Nbs demonstrated an avidity effect. Interestingly, the binding of HJ-2x2Rb17c to SkBr3 cells demonstrated a 15-fold increase compared with the monovalent counterpart, whereas HJ-2x2Rs15d exhibited a 2.4-fold increment. Notably, the biparatopic HJ-2Rs15d-2Rb17c exhibited the strongest binding, being up to 25-fold higher than the monovalent HJs and 1.4- and 1.6-fold higher than observed for the HJ-2x2Rs15d and HJ-2x2Rb17c, respectively, although not statistically significant. Moreover, both the homobivalent and biparatopic HJ constructs were able to detect the lower levels of HER2 on MCF-7 and the extremely low expression on MDA-MB-231 cells, with the biparatopic construct being the most sensitive among all the tested constructs.

Of note, the degree of cell binding was independent of the spatial arrangement of the Nbs on the HJ scaffold as shown by flow
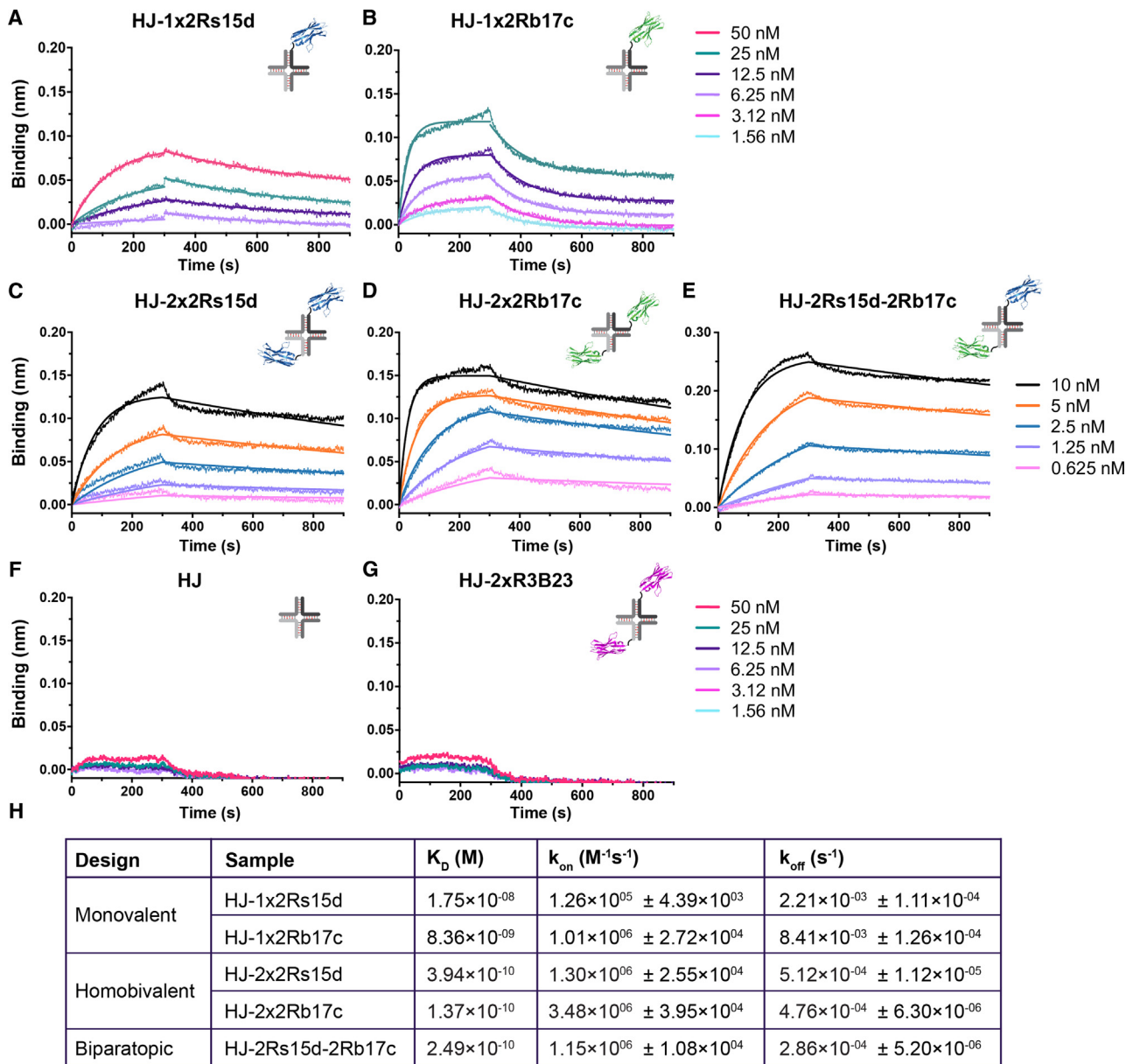
Figure 2. Binding kinetics of the anti-HER2 HJs to the HER2 receptor

(A–G) BLI sensorgrams of the association and dissociation curves of the anti-HER2 and negative control HJs at the indicated concentrations: (A, B, F, and G) 50–1.56 nM; (C–E) 10–0.625 nM. The binding curves were fitted and the K_D, k_{on}, and k_{off} values were calculated for each construct and provided in (H) (for details see materials and methods). The BLI profiles shown in this figure are representative of three individual tests.

Design	Sample	K_D (M)	k_{on} (M^{-1}s^{-1})	k_{off} (s^{-1})
Monovalent	HJ-1x2Rs15d	1.75×10^{-08}	$1.26 \times 10^{05} \pm 4.39 \times 10^{03}$	$2.21 \times 10^{-03} \pm 1.11 \times 10^{-04}$
	HJ-1x2Rb17c	8.36×10^{-09}	$1.01 \times 10^{06} \pm 2.72 \times 10^{04}$	$8.41 \times 10^{-03} \pm 1.26 \times 10^{-04}$
Homobivalent	HJ-2x2Rs15d	3.94×10^{-10}	$1.30 \times 10^{06} \pm 2.55 \times 10^{04}$	$5.12 \times 10^{-04} \pm 1.12 \times 10^{-05}$
	HJ-2x2Rb17c	1.37×10^{-10}	$3.48 \times 10^{06} \pm 3.95 \times 10^{04}$	$4.76 \times 10^{-04} \pm 6.30 \times 10^{-06}$
Biparatopic	HJ-2Rs15d-2Rb17c	2.49×10^{-10}	$1.15 \times 10^{06} \pm 1.08 \times 10^{04}$	$2.86 \times 10^{-04} \pm 5.20 \times 10^{-06}$

cytometry with the 2Rb17c Nb positioned either adjacent (on the Q3 module) or opposite (on the Q4 module) to the 2Rs15d Nb (Figure S2).

Encouraged by the performance of both the homobivalent and biparatopic HJs in the flow cytometry studies, we examined their potential as detection probes for *in vitro* diagnostics of breast cancer. In the clinic today, *in situ* antibody staining combined with microscopy is commonly used to distinguish HER2-positive breast cancer. Here,

we employed 3,3′-diaminobenzidine (DAB) staining for immunocytochemistry (ICC) using different HJ-Nb constructs, which were assembled with a biotin-modified Q2 module for detection by a streptavidin-horseradish peroxidase (HRP) polymer (Figure S3).

For ICC, the previously mentioned three cell types were stained with either naked HJ or HJ-2xR3B23 as negative controls or the strong binders, HJ-1x2Rs15d, HJ-2x2Rs15d, HJ-2x2Rb17c, and the
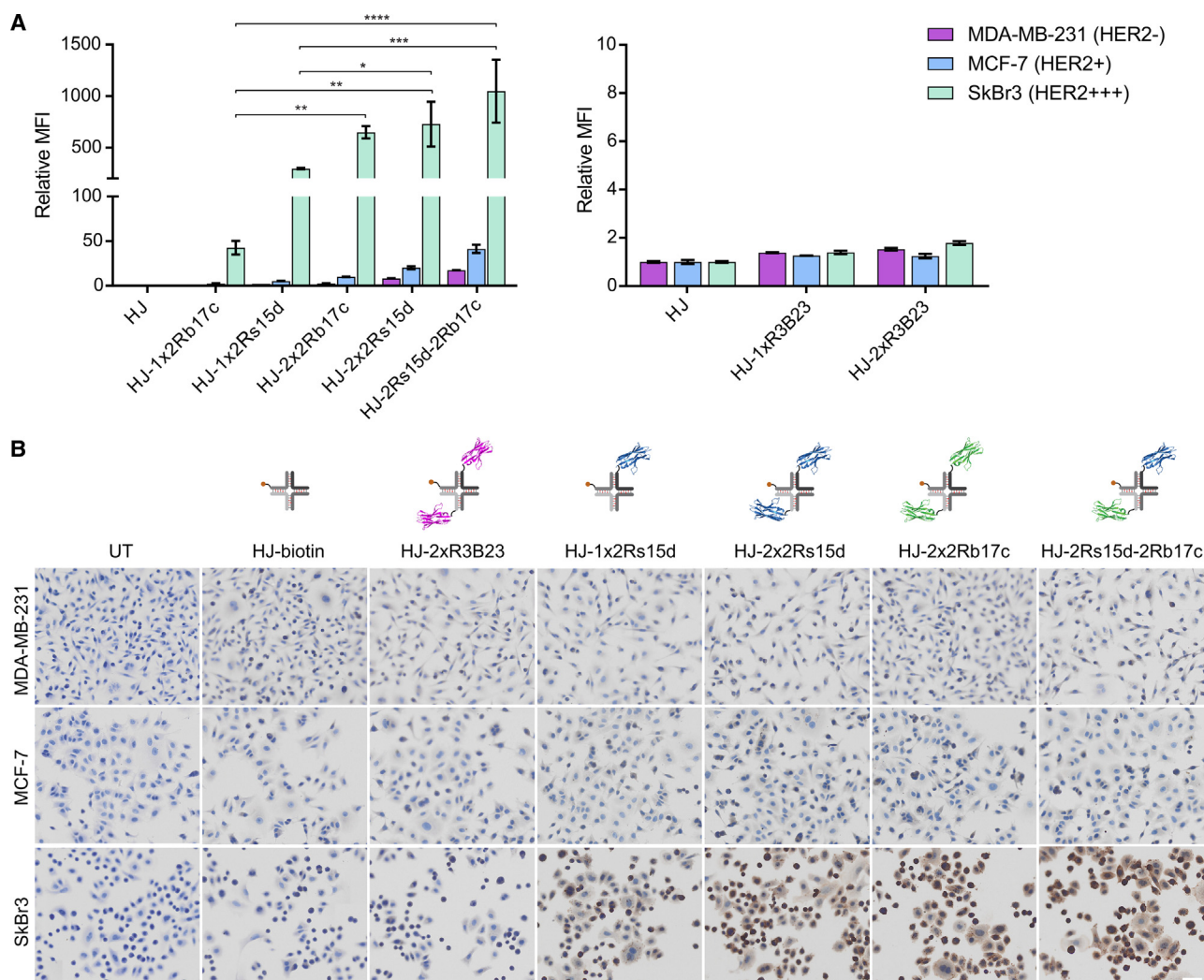
Figure 3. Binding and detection of HER2 in breast cancer cell lines with the anti-HER2-HJs

(A) Binding of anti-HER2 and negative control HJs for the three cell lines, SkBr3 (HER2+++), MCF-7 (HER+), and MDA-MB-231 (HER2–). The bars represent the median fluorescence intensity (MFI) from cells stained by each construct normalized to the MFI of cells stained by the naked HJ. For comparison of multiple groups in SkBr3 cells, statistical analysis was conducted using one-way ANOVA followed by Tukey's post-hoc test. Error bars represent mean ± standard deviation (SD). $*p = 0.0457$, $**p < 0.005$, $***p = 0.0007$, and $****p < 0.0001$. (B) ICC images of DAB-stained breast cancer cells following the incubation with biotin-modified anti-HER2 and negative control nanostructures. Scale bar, 50 μm.

biparatopic HJ construct (Figure 3B). Again, the staining intensity of the HJs between cell lines followed HER2 expression levels. While specific binding was confirmed by the absence of visible DAB staining in the negative control groups, SkBr3 cells showed strong binding for all anti-HER2 HJs with a slightly stronger coloration for the biparatopic construct. For the lower HER2 expression cell lines, MCF-7 and MDA-MB231, no apparent variation was observed when cells were subjected to staining with the monovalent HJs compared with untreated or HJ-biotin groups. Staining with either homobivalent or biparatopic HJs resulted in a slightly darker signal intensity, particularly for MCF-7 cells.

These results demonstrate that the multimerization of Nbs and the ability to target two specific epitopes on the HER2 receptor sub-

stantially enhances their binding and specificity to HER2-positive cells.

SPECT-CT imaging of anti-HER2-HJs in HER2-positive mouse xenografts

The significant enhancement in binding capabilities of both homobivalent and biparatopic anti-HER2 HJs, along with their stability in serum for up to 24 h (Figure S4), encouraged the use of these constructs as tracers for *in vivo* nuclear imaging. To verify the biocompatibility of the nanostructure, its immunogenicity was assessed by measuring concentrations of tumor necrosis factor-alpha (TNF-α) and interferon-gamma (IFN-γ) released by peripheral blood mononuclear cells (PBMCs) upon exposure. After incubating PBMCs
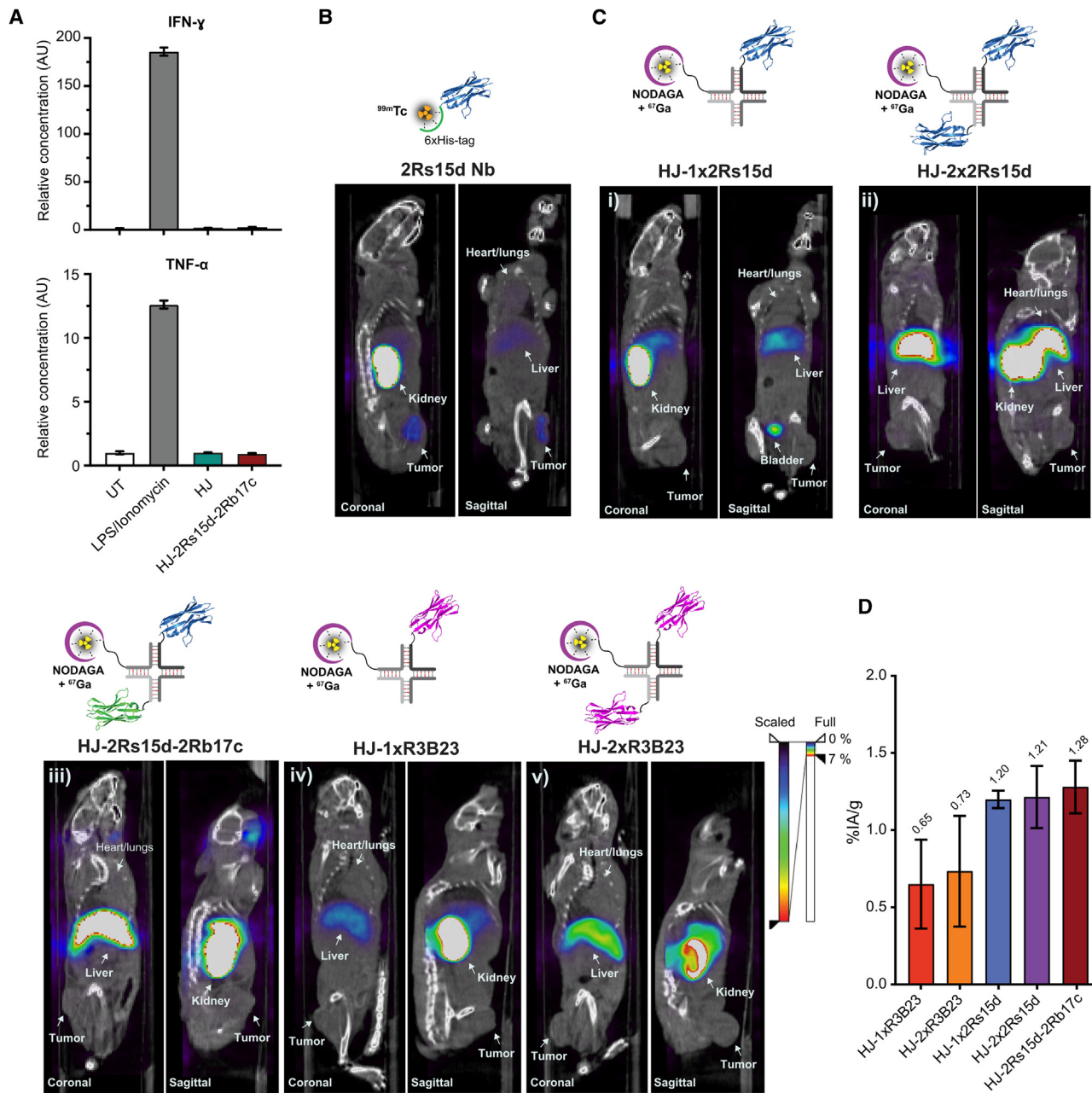
Figure 4. *In vivo* SPECT-CT imaging and biodistribution of anti-HER2-HJs

(A) Relative concentration of IFN-γ and TNF-α released by human PBMCs in response to HJ or HJ-2Rs15d-2Rb17c constructs. Data are normalized to the untreated control (UT) and presented as mean (SD). Positive control group consists of LPS (5 μg/mL) and ionomycin (5 mM). (B) The HER2 expression of SKOV3 tumors was verified by SPECT-CT imaging 1 h (h) after injecting xenografted mice i.v. with ^{99m}Tc-labeled 2Rs15d Nb. (C) The retention of the ^{67}Ga-labeled anti-HER2 and negative control HJs was visualized by SPECT-CT imaging (i, ii, and iii) 1 h after i.v. injection in xenografted mice. (D) *Ex vivo* measurement of tumor accumulation was reported as the percentage of injected radioactivity/gram (% IA/g) of dissected tumors. Bars indicate mean (SD) of $n = 3$ mice per group. SPECT-CT images were processed by using the Amide software. The NIH+ white color table was set with maximum threshold: 7% (see scale), while CT images were visualized using the color table black/white/black with maximum threshold: 100%.

with the construct for 24 h, the results revealed that the anti-HER2 HJ induced levels of TNF-α and IFN-γ (Figure 4A) comparable with those observed for untreated PBMCs. In contrast, high

levels of both cytokines were induced when incubated with immunogenic lipopolysaccharides (LPSs) and ionomycin, used as positive controls.

Based on the *in vitro* screening and their non-immunogenic profile, the mono- and homobivalent 2Rs15d-bearing HJs along with the biparatopic anti-HER2 HJ were chosen to be the best-performing configurations for further screening in mice.

To test the tumor-targeting potential of the anti-HER2 HJs, we inoculated SKOV3 cells subcutaneously in nude mice to form HER2-positive tumor xenografts. To verify HER2 expression in the tumors, the single 2Rs15d Nb was radiolabeled with technetium-99m (^{99m}Tc) through chelation to the C-terminal His-tag of the Nb (Figure S5) and was subsequently injected intravenously (i.v.) in the xenografted mice. The accumulation of the ^{99m}Tc-labeled 2Rs15d Nb tracer (referred to in supplemental figures as 2Rs15d-N$_3$-6xHis-[^{99m}Tc]Tc) was visualized after 1 h by single-photon emission computed tomography combined with computed tomography (SPECT-CT) and quantified *ex vivo* after 1.5 h, upon dissection analysis (Figures 4B and S6). The Nb tracer confirmed the HER2 expression of tumor xenografts and *ex vivo* measurements of tumors revealed an accumulation of 4.5% ± 0.9% of injected activity per gram of dissected tissue (% IA/g). Similarly to the wild-type Nb,[37] the biodistribution of the azido-modified Nb showed a high kidney accumulation (Figure S6), indicating that its elimination from the blood is prevalently mediated by renal clearance.

For the radiolabeling of the HJ constructs with gallium-67 (^{67}Ga), the Q2 module was functionalized with the NODAGA chelator to produce [^{67}Ga]Ga-NODAGA-Q2 (Figure S7). The [^{67}Ga]Ga-NODAGA-Q2 was assembled with the remaining HJ modules in equimolar amounts to form the desired configuration of ^{67}Ga-labeled HJ-1x/2xNb constructs (referred in supplemental figures as [^{67}Ga]Ga-HJ-1x/2xNb), which were subsequently purified to remove any trace of free ^{67}Ga and validated by radio size-exclusion HPLC (radio-SEC-HPLC) (Figures S8–S10). Native gel analysis of the ^{67}Ga-labeled HJ constructs revealed no indications of degradation or aggregation products after 8 h incubation in injection buffer at room temperature (RT), suggesting that the nanostructures were intact, stably radiolabeled, and monodisperse in solution before their injection (Figure S11).

The ^{67}Ga-labeled HJ-1x2Rs15d, HJ-2x2Rs15d, HJ-2Rs15d-2Rb17c, and the negative control HJ-1x/2xR3B23, were injected i.v. in nude mice bearing HER2-positive tumor xenografts and SPECT-CT imaging and dissection analysis were performed at 1 and 1.5 h post-injection, respectively. The blood signal measured *ex vivo* reached background levels (Figure S12), indicating that the HJ constructs were cleared from blood after 1.5 h. A high kidney accumulation was visualized by SPECT-CT scans (Figure 4C) and measured *ex vivo* to be between 32% and 38% IA/g (Figure S12), confirming a predominant renal clearance due to the estimated small size of the constructs (naked HJ ∼16 kDa, monovalent HJ-Nb ∼30 kDa, bivalent or biparatopic HJ-Nb ∼44 kDa).

Liver and spleen accumulation was also visible in SPECT-CT scans (Figure 4C) and was confirmed by *ex vivo* measurements revealing a signal ranging between 2% and 7% IA/g for all the constructs (Figure S12). The rest of the non-targeted tissues maintained a background signal between 0% and 3% IA/g.

Although we did not detect any visible signal from the tumor xenografts in SPECT-CT scans, the *ex vivo* measurements demonstrated 1.7-fold greater tumor retention of all three anti-HER2 HJs compared with the mono- and homobivalent negative control HJs (Figure 4D). However, tumor accumulation of the anti-HER2 constructs was not significantly changed depending on the different Nb configurations, as it ranged from 1.20% ± 0.05% IA/g for the HJ-1x2Rs15d, to 1.28% ± 0.17% IA/g for the biparatopic construct. Furthermore, the relative tumor retention from the *ex vivo* measurements of the HER2-targeting nanostructures was 3.5-fold lower than that observed for the single 2Rs15d Nb.

While these findings do not conclusively inform about the optimal Nb configuration for tracer imaging of HER2 *in vivo*, they illustrate construct-specific behavior and the complexity of harnessing Nb multimers as tracers for molecular imaging.

DISCUSSION

Image contrast and signal-to-noise ratio determine the quality and resolution of molecular imaging. These factors can be directly influenced by the binding characteristics of the imaging agent, such as Nbs. In this study, we demonstrate an efficient and reliable plug-and-play method for multimerizing clinically relevant Nbs on our nucleic acid-based HJ platform to significantly increase their binding strength and improve HER2 detection.

The HER2 receptor is an established biomarker for cancer cells and can be targeted by, among others, two previously reported Nbs, 2Rs15d and 2Rb17c.[37] Because the 2Rs15d and 2Rb17c Nbs bind two non-overlapping epitopes of the HER2 receptor, we speculated that multimerization of the Nbs, especially in a biparatopic display, would increase the avidity of the Nbs toward HER2. Hypothetically, one homobivalent HJ could bind to one receptor monomer or simultaneously interconnect two receptors on a HER2 dimer, whereas two heterobivalent biparatopic HJs should be able to bind the same monomer, therefore increasing the number of bound nanostructures to the single target protein.

The systematic screening of the binding kinetics of various multimerized Nb configurations by BLI, demonstrated the retained HER2-specific binding of the Nbs upon oligonucleotide conjugation and assembly into HJ-Nb constructs and further confirmed the expected improved binding stability and avidity of homobivalent and biparatopic anti-HER2 Nbs. The best results were obtained with the homobivalent and the biparatopic constructs, HJ-2x2Rb17c and HJ-2x2Rs15d-2Rb17c, respectively. Owing to the synergistic effect of two Nbs, the off-rate (k_{off}) for the homobivalent HJ-2x2Rb17c construct was improved by nearly two orders of magnitude in comparison with its monovalent counterpart. The biparatopic construct was able to successfully combine the fast-binding feature of the 2Rb17c Nb and the association stability of

the 2Rs15d Nb, for an overall enhanced binding relative to the monovalent and homobivalent HJ-Nbs. Both constructs produced highly performant binding nanostructures capable of stronger and more enduring association with HER2 receptors.

These effects were also evident from cell binding experiments, where the extent of binding was highly specific to the receptor expression of three different cell lines. In particular, the signal obtained by the HER2+++ cells emphasized the different avidity of the anti-HER2 HJ constructs, confirming that the homobivalent and biparatopic display of Nbs significantly enhanced the targeting power of the HJ nanostructures. Interestingly, both combinations were effective in detecting very low levels of the receptor, as seen for the MCF-7 and MDA-MB-231 cells, which are typically challenging to detect by antibody-based staining methodologies.[42,45] These results, particularly achieved with the biparatopic HJ, suggested an exceptionally stronger detection capacity in terms of sensitivity and specificity, which confers a robust potential as a more precise antigen detector, i.e., for *in situ* diagnostic purposes. The facile plug-and-play conversion of the HJ nanoscaffold to any type of detection system, here demonstrated by DAB staining for ICC, encourages their application potential in colorimetric or fluorescent immunohistochemistry that may be extended to tissue samples.

To investigate the possible imaging applications of the system *in vivo*, we demonstrated the serum stability and biocompatibility of the anti-HER2 HJs, and we adapted the nanostructure for detection in nuclear imaging. Due to the modularity of the HJ scaffold and undemanding functionalization protocol, we were able to investigate several radiolabeled nanostructure combinations for SPECT-CT imaging of mice xenografted with HER2-positive tumors. Although visible tumor targeting was not observed from SPECT-CT imaging, *ex vivo* measurements of the dissected tumors indicated a higher accumulation of the ^{67}Ga-labeled anti-HER2 HJs with respect to negative control HJ constructs. However, compared with the free ^{99m}Tc-labeled 2Rs15d Nb, the anti-HER2 HJs exhibited lower tumor retention. This result is likely connected to the difference in biodistribution and clearance pathways characterizing the free 2Rs15d Nb and the constructs, as it played a determining role in maintaining a sufficient bioavailability of circulating tracers. We believe that the modest tumor localization of the HJ constructs is primarily due to low bioavailability as a result of rapid blood clearance and evident accumulation in the liver and spleen. Nucleic acids are known to be cleared from the blood by the reticuloendothelial system (also known as the mononuclear phagocyte system [MPS]) following opsonization.[46–48] It is speculated that the substantial reduction in the blood half-life of our HJ-Nb constructs may be driven by the association of serum proteins that lead to the formation of a protein corona. Not only may this shield and prevent the multimerized Nbs from binding to their target tissue, it could also trigger the sequestration of opsonized nanostructure in MPS organs, such as the liver and spleen. Another factor that might have played a role in the biodistribution of the HJ constructs, and the lack of tumor targeting, is the incremented size of the bivalent nanostructures in comparison with the single Nb. While the free Nb is predominantly cleared by renal secretion, the resulting size of the multimerized constructs (estimated to be 8–10 nm) likely overcame the threshold for clearance by the glomerular filtration membrane, which is known to be 6–8 nm.[49] This feature is desired as it should reduce renal clearance and prolong the circulation time of the multimerized Nbs, improving chances for the nanostructure to reach and bind the target tissue. However, the incremented size could potentially reduce the penetrability of the construct in tumor tissues, while the longer circulation time increases the exposure to the MPS cells in the liver and spleen,[50] known to be responsible for the uptake of foreign particles.[51] Despite our lack of more in-depth knowledge of the short blood half-life and the exact clearance mechanisms characterizing the HJ-Nb constructs, we envision that the bioavailability and biodistribution of the nanostructures could be improved by further modification of the HJ scaffold. This could for example be achieved by introducing pharmacokinetic enhancers on the last available module (Q3) that remained unmodified in all our tested constructs. It has been demonstrated previously that the half-life of the HJ nanoscaffold can be tuned through functionalization with polyethylene glycol (PEG) moieties of varying sizes.[39] PEGylation can both shield the negative surface charge of the nucleic acid-based scaffold from opsonin-mediated adsorption and reduce the uptake by the cells of the MPS.[52,53] Both actions, along with the further increase in the hydrodynamic size, would prolong the blood circulation time and bioavailability of the HJ-Nb constructs. However, administration of PEGylated nanomaterials has also been associated with immunogenic response which may cause adverse side effects for *in vivo* applications.[54] Cholesterol or other hydrophobic molecules can alternatively be used to enhance the pharmacokinetics of the HJ constructs through binding to serum albumin.[55]

This study demonstrates an improvement in target binding by creating a bivalent and biparatopic Nb display through the effect of avidity. The expression system adopted to produce Nbs for site-specific conjugation,[20] combined with the modularity of the HJ scaffold, offered a powerful plug-and-play approach to explore several targeting combinations against HER2. The method is not limited to HER2 but applies to targeting any pathology with a known associated biomarker. In contrast to functionalizing mAbs, the possibility to conjugate dyes, chelators, and other molecules, such as biotin, with precise stoichiometry, makes the HJ-Nb a competitive platform technology.

Furthermore, the biparatopic configuration of anti-HER2 HJ-Nbs has the potential to inhibit HER2 dimer formation and block downstream tumor signaling, therefore offering a therapeutic effect[56] with respect to single Nbs or antibodies. Moreover, as similar technologies have shown promising therapeutic applications,[57] payloads such as therapeutic radionuclides, drugs, or toxins, could be used to further functionalize the anti-HER2 HJs already coupled to a detection element, thereby creating a targeted theranostic device.

MATERIALS AND METHODS
Primary Nb sequences
The amino acid sequences for the Nbs employed in this study are listed below. The letter X in bold designates the position of the unnatural amino acid 4-azido-L-phenylalanine.

2Rs15d;

QVQLQESGGGSVQAGGSLKLTCAASGYIFNSCGMGWYRQSPGR
ERELVSRISGDGDTWHKESVKGRFTISQDNVKKTLYLQMNSLKP
EDTAVYFCAVCYNLETYWGQGTQVTVSSAAA**X**GSHHHHHH

2Rb17c;

QVQLQESGGGLVQPGGSLRLSCAASGFIFSNDAMTWVRQAPGKG
LEWVSSINWSGTHTNYADSVKGRFTISRDNAKRTLYLQMNSLKDE
DTALYYCVTGYGVTKTPTGQGTQVTVSSAAA**X**GSHHHHHH

R3B23;

MKYLLPTAAAGLLLLAAQPAMAQVQLQESGGGLVQPGGSLRLS
CAASGFIFSNDAMTWVRQAPGKGLEWVSSINWSGTHTNYADS
VKGRFTISRDNAKRTLYLQMNSLKDEDTALYYCVTGYGVTKTP
TGQGTQVTVSSAAA**X**GSHHHHHH

Nb expression and purification

The anti-HER2 Nbs, 2Rs15d and 2Rb17c,[37] and the anti-5T2 multiple myeloma Nb R3B23[41] (used as negative control) were expressed in *E. coli* with a site-specific azido group positioned at the C-terminal for orthogonal copper-free click reaction, as reported previously.[20] In brief, each Nb sequence is modified with an N-terminal pelB sequence and C-terminal amber (TAG) stop codon followed by a hexahistidine tag (6xHis tag). The Nb sequence was cloned into pMECs plasmid and together with pUltra suppressor plasmid co-transformed in *E. coli*. A discrete colony was grown in TB medium at 37°C, 220 rpm. At optical density (OD) 0.8 < OD < 0.9, 4-azido-L-phenylalanine was added to the culture to a final concentration of 1 mM (corresponding to 0.202 g/L) followed by the addition of IPTG to a final concentration of 1 mM. The culture was then grown at 18°C reaching a total of 16 h of incubation. The Nb was harvested by periplasmic extraction and purified by Ni-NTA affinity chromatography using Äkta Start System (Cytiva). Nbs were buffer-exchanged against 1× PBS using Amicon Ultra 3K spin-filters (Merck Millipore).

Nb-oligonucleotide bioconjugation and purification

The 2′-OMe- and LNA-modified HJ Q modules[39] were purchased from Integrated DNA Technologies (IDT). The modules destined for Nb functionalization were modified with a 5′ dibenzocyclooctyne (DBCO) handle for subsequent copper-free click reaction with azido-modified Nbs. In brief, the Q1, 3, and 4 modules were reacted with a hetero-bivalent linker, NHS-DBCO (Sigma-Aldrich), in a 1:50 ratio in 100 mM HEPES buffer (pH 8.2) and 60% DMSO, at RT, 600 rpm for 4.5 h. Excess NHS-DBCO was removed by ethanol (EtOH) precipitation and the oligonucleotides were re-suspended in nuclease-free (NF) water before reverse-phase HPLC purification (RP-HPLC). Fractions containing DBCO-modified modules were collected, freeze-dried, and resuspended in NF water before spectrophotometric quantification on a Nanodrop (DeNovix).

Azido-Nbs were conjugated to DBCO-modules in an SPAAC reaction using a 2:1 ratio RT at 600 rpm overnight (O/N). The reaction efficiency and purity of Nb-oligonucleotide bioconjugates were verified by both 12% denaturing PAGE and SDS-PAGE (NuPAGE 4%–12%, Bis-Tris, Thermo Fisher Scientific).

The Nb-oligonucleotide bioconjugates were purified from 1% agarose gel run at 120 V for 1.5 h. The band containing the bioconjugate was visualized under UV light and cut out from the gel. The gel piece was added to a dialysis membrane tube (3.5 kDa cutoff, Spectra/Por3, 132724), precendently soaked in 1× Tris-borate-EDTA buffer (1× TBE) for 10 min and then filled with 1× TBE and sealed. The sealed tube was immersed into an electrophoresis chamber with the gel piece perpendicular to the electric field. A voltage of 120 V was applied for 15–20 min until the conjugate had run out of the gel. The buffer containing the bioconjugates was collected from the dialysis tube. The bioconjugates were concentrated and buffer exchanged against 1× PBS Amicon Ultra 10K spin-filters (Sigma-Aldrich).

Q2 module functionalization for detection purposes

For detection by gel electrophoresis, flow cytometry, and immunocytochemistry, HJs were assembled with the Q2 module carrying a fluorescent dye and biotin, respectively. This was conducted by reacting the Q2 module with either NHS-Cy5, NHS-Alexa Fluor 647 (AF647), or NHS-biotin in a 1:5 and 1:50 ratio, respectively, in 100 mM HEPES buffer (pH 8.2) and 60% DMSO, at RT, 600 rpm for 4.5 h. Prior to RP-HPLC purification, excess NHS-dye/biotin was removed by EtOH precipitation. The fractions holding the final conjugates were collected and lyophilized O/N, reconstituted in NF water, and quantified spectrophotometrically.

For *in vivo* nuclear imaging, HJs were assembled with a Q2 module functionalized with a 1,4,7-triazacyclononane,1-glutaric acid-4,7-acetic acid (NODAGA) chelator. The Q2 module was reacted with NHS-PEG5-methyltetrazine (MeTz) (Conju-probes CP-6062) in a 1:20 ratio in 100 mM HEPES buffer (pH 8.2) and 60% DMSO, at RT, 700 rpm for 4.5 h. Excess NHS-PEG5-MeTz was removed by EtOH precipitation and conjugates were resuspended in Fluka water (Honeywell). 5′-MeTz-PEG5-Q2 were then reacted to bicyclononyne-NODAGA (CheMatech, dissolved in 100 mM NaOAc [pH 4.4–4.6]) in a 1:2 ratio at pH 7.6, adjusted by adding 0.2 M Na$_2$CO$_3$. The reaction was carried out at RT, 600 rpm for 4 h. NODAGA-Q2 conjugates were thoroughly washed by EtOH precipitation and resuspended in Fluka water.

Gel electrophoresis

Reaction products were analyzed using PAGE gels. Denaturing PAGE gels (12% polyacrylamide) were prepared using 17 mL UreaGel Diluent (National Diagnostics), 19 mL UreaGel Concentrate (National Diagnostics), and 4 mL 10× TBE (Gibco by Life Technologies), 420 μL ammonium persulfate (APS) (Sigma Aldrich), and 20 μL TEMED (Sigma-Aldrich). The gels were pre-run at 600 V for 30 min before loading the samples. Native PAGE gels (10% polyacrylamide) contained 10 mL Accugel 29:1 (40%, National Diagnostics)

4 mL 10× TBE (Gibco by Life Technologies), 26 mL Milli-Q water, 420 μL 10% APS, and 20 μL of TEMED. All PAGE gels were stained with SYBR Gold (Invitrogen) in Milli-Q water for 10 min and scanned on an Amersham Typhoon 5 scanner (GE Healthcare), including the detection of the conjugated fluorescent dye when necessary.

Radiolabeled HJs were loaded in 10% polyacrylamide native Novex TBE Gels (Invitrogen, EC6275BOX) and run in 1× TBE buffer at 100 V for 1.5 h. The gels were stained with SYBR Gold and scanned using an Amersham imager 680. The radioactive signal of the HJs was visualized by phosphorimaging using a Typhoon FLA 7000 (GE Healthcare) upon O/N exposure.

For protein detection, a NuPAGE 4%–12% Bis-Tris gel (Thermo Fisher Scientific) was run in MES buffer at 150 V for 40 min and subsequently stained with Coomassie brilliant blue and destained in Milli-Q water O/N before scanning on a GelDoc Ez Imager (Bio-Rad).

For gel purification, 1% agarose was prepared by adding 1 g of agarose (Invitrogen) to 100 mL of 1× TBE. The mix was dissolved in a microwave followed by the addition of SYBR Safe prior to gelation.

Ultralow-range DNA ladder (10–300 bp, Thermo Scientific) was used as a size marker for the denaturing and native PAGE gels, while PageRuler Plus Prestained Protein Ladder cat. no. 26619 (Thermo Fisher Scientific) was used for SDS-PAGE.

Radiolabeling procedure and quality control

$[^{67}Ga]GaCl_3$ was obtained from $[^{67}Ga]Ga$-citrate as described previously.[58] In brief, $[^{67}Ga]Ga$-citrate diluted in Fluka water was applied to a SEK-PAK Vac 1 cc (100 mg) silica cartridge (Waters) using the Reglo Independent Channel Control peristaltic Pump (Ismatec) and 0.13 mm tubings. Citrate ions were removed by flushing Fluka water and the retained radioactivity was eluted in six 50 μL fractions by applying 0.1 M HCl. Three fractions containing the highest radioactivity were pooled together reaching 412 MBq. Radiolabeling with ^{67}Ga ($t_{1/2}$ = 78.3 h) of the 5′-NODAGA-Q2 was performed as described previously by Bridoux et al.[18] A single 5′-NODAGA-Q2 labeling reaction was prepared for each final HJ configuration. Radiolabeling was carried out at 100 μM final concentration of 5′-NODAGA-Q2 in 35 μL of the final volume. The oligonucleotide was mixed with NH_4Oac pH 5.4 (final concentration 0.568 M) and incubated for 5 min at 50°C, followed by the addition of $[^{67}Ga]GaCl_3$ and incubation for 10 min at 50°C. Radiolabeling efficiency was verified by radio-iTLC and radio-SEC-HPLC. Each 5′-$[^{67}Ga]Ga$-NODAGA-Q2 radiolabeling reaction mix was added to each correspondent one-pot HJ assembly mix only after all the other HJ components were already added. For quality control, ~2 MBq of $[^{67}Ga]Ga$-NODAGA-Q2 or fully assembled $[^{67}Ga]Ga$-HJ-1x/2x Nb was diluted in citrate-Tween 20 buffer (0.1 M Na citrate and 0.1% Tween 20) and loaded for radio-SEC-HPLC using a Superdex 75 Increase 5/150 GL column (Cytiva) during a 12 min run at 0.45 mL/min in 2× PBS. The time delay in detecting UV and radioactivity exhibited

in radio-SEC-HPLC chromatograms reported in Figures S7–S10 results from the placement of the radio detector downstream of the UV detector.

The radiolabeling of the 2Rs15d-azide Nb was performed by using the C-terminal 6xHIS tag as a chelator. The ^{99m}Tc-tricarbonyl intermediate $[99mTc(H_2O)_3(CO)_3]$ was synthesized using the Isolink labeling kit (Mallinckrodt Medical BV, Petten, the Netherlands). Radio-iTLC was performed by using 0.1 M Na citrate. The Nb was filtered through a PD-10 desalting column (Cytiva) and buffer-exchanged against 1× PBS. For quality control, about 2 MBq of ^{99m}Tc-labeled 2Rs15d was diluted in buffer A, H_2O + 0.1% trifluoroacetic acid (TFA), and loaded for radio-RP-HPLC using a PLRP-S 5 μm 250 × 4.6 mm column (Agilent) at 1 mL/min, through an increasing concentration of buffer B (acetonitrile + 0.1% TFA) following a gradient method (0–5 min = 25% B; 5–7 min = 25%–34% B; 7–10 min = 34%–100% B; 10–22 min = 100% B; 22–27 min = 25% B). The expected retention time of the Nb is 12 min. The time delay in detecting UV and radioactivity exhibited in the RP-HPLC chromatogram reported in Figure S5 results from the placement of the radio detector downstream of the UV detector.

HJ assembly and quality control

The four required HJ modules among 5′-NH_2-Q2/3/4, AF647/biotin/-Q2, and Nb-Q1/2/4 were added in a one-pot assembly mix in equimolar amounts in 1× PBS to assemble each desired HJ. Once thoroughly mixed, the HJs were incubated at RT O/N. The assembly of unlabeled or fluorescently labeled HJs was validated by native PAGE.

The ^{67}Ga-labeled HJs destined for *in vivo* nuclear imaging were assembled upon 5′-NODAGA-Q2 radiolabeling with ^{67}Ga. The four HJ modules constituting each configuration (5′-NH_2-Q3, $[^{67}Ga]Ga$-NODAGA-Q2, and Nb-Q1/4) were added in a one-pot assembly mix in equimolar amounts in 1× PBS and incubated O/N at RT. The ^{67}Ga-labeled HJs were buffer-exchanged against 1× PBS through SEC filtration using a Nap-5 pre-packed Column Sephadex G-25 (GE Healthcare). For quality control, ~2 MBq of each ^{67}Ga-labeled HJ construct was diluted in citrate-Tween 20 buffer and loaded for SEC-HPLC using a Superdex 75 Increase 5/150 GL column (Cytiva) in a 12 min run at 0.45 mL/min in 2× PBS.

HJ stability studies

The HJ-2Rs15d-2Rb17c nanostructure and the naked HJ scaffold were used to test the stability in serum of the Nb-functionalized HJs labeled with AF647 dye. A total of 2 pmol of pre-assembled HJ was added to 8 μL 1× PBS or 10% FBS in 1× PBS (corresponding to a final HJ concentration of 250 nM) and incubated on a thermoblock at 37°C. At the time points 0 and 30 min, and 1, 2, 6, and 24 h, samples were flash-frozen in dry ice and successively stored at −20°C. The stability of the constructs was visualized by native PAGE.

The stability in the injection buffer of the ^{67}Ga-labeled HJ constructs was tested by incubating the radiolabeled nanostructures in 1× PBS at

RT for 8 h. The stability of the several constructs was visualized by native PAGE.

BLI binding assay

The binding kinetics of the HJ constructs were studied with BLI using OCTET red96e (ForteBio). Samples dilution was performed by using $1\times$ PBS with 0.01% Tween 20 and 0.1% BSA (PBSTB). The same buffer was used to measure all the baselines and references. To explore binding kinetics, negative control and monovalent constructs were diluted from 50 to 1.56 nM by a 2-fold serial dilution while all the bivalent anti-HER2 constructs were titrated from 10 to 0.625 nM. All measurements were carried out at RT, 1,000 rpm in 96-well plates (black, flat bottom, Greiner). The Fc-Her2 receptor (Sino Biological, cat. no. 10004-H02H), 2 µg/mL, was immobilized on anti-hIgG Fc-capture sensors (Sartorius, 18-5060) by a 600 s loading step. Before all binding measurements, a baseline was run for 60 s in PBSTB, followed by a 300 s association phase and a 600 s dissociation phase. Sensors were regenerated after each binding measurement by 5 cycles of stripping in 10 mM glycine buffer (pH 1.7) for 5 s and 5 s washing in PBSTB. Binding curves were aligned to the baseline and reference wells were subtracted. Curve fits were performed by using GraphPad Prism 10.0.1. The association and dissociation curves relative to the monovalent anti-HER were separately fit in a global 1:1 model by using the rate constant "K" obtained from the "dissociation-one phase exponential decay" fit model, as constrained k_{off} for the following "association kinetics-two or more conc. of hot" fit model. The bivalent anti-HER2 HJ binding curves were also globally fit to a 1:1 model by using the "association and dissociation" model. The non-specific signal was constrained to 0.

Cell lines

The SkBr3 cell line was cultured in McCoy's 5a medium modified (Gibco, 16600082), while the MCF-7 and MDA-MB-231 cells were cultured in DMEM. All media were supplemented with 10% fetal bovine serum (FBS) and 1% penicillin/streptomycin. Cells were cultured at $37^{\circ}C$ in a humidified atmosphere with 5% CO_2. Tumor xenografts were prepared by culturing SKOV3 cells in RPMI medium supplemented with 10% FBS, 2 mM L-glutamine, 100 U/mL penicillin, and 0.1 mg/mL streptomycin. Cells were cultured in a humidified atmosphere with 5% CO_2 at $37^{\circ}C$ and prepared for *in vivo* subcutaneous injections by detaching them using trypsin-EDTA (Life Technologies) and resuspending them in $1\times$ PBS.

Flow cytometry studies

Each well of a 24-well plate was seeded with 100,000 cells suspended in supplemented medium and incubated O/N. The following day, the medium was removed and adherent cells were washed with $1\times$ PBS. Cells were then incubated at RT for 30 min in supplemented medium containing 20 nM of HJ constructs (staining medium). Upon removal of the staining medium, cells were washed in $1\times$ PBS and 500 µL of trypsin-EDTA was added and incubated at $37^{\circ}C$ for 3–5 min. The same volume of supplemented medium was added to stop the action of trypsin. Cells were collected in separate tubes and washed three times with $1\times$ PBS by centrifuging for 10 min at $2,000 \times g$. The su-

pernatant was removed, and cells were resuspended in $1\times$ PBS for flow cytometry analysis. The median fluorescence intensity (MFI) from cells stained by each construct was normalized to the MFI of cells stained by the naked HJ. For comparison of multiple groups in SkBr3 cells, statistical analysis was conducted using one-way ANOVA followed by a Tukey's post-hoc test. Error bars represent mean ± SD. $*p = 0.0457$, $**p < 0.005$, $***p = 0.0007$, and $****p < 0.0001$.

Immunocytochemistry studies

Biotinylated anti-HER2-HJs were used to perform ICC staining on cells expressing different levels of HER2 receptors. SKOV3, MDA-MB-231, and MCF7 cells were cultured on a glass-bottom slide with a removable 12-well chamber (Ibidi, cat. no. 81208). After 48 h, cells were fixed in a 4% formaldehyde solution at RT for 10 min followed by three washing steps for 5 min in $1\times$ PBS supplemented with 1 mM $CaCl_2$, 0.5 mM $MgCl_2$, and 0.05% Tween 20 (onward referred to as wash buffer). To block the endogenous peroxidase activity, cells were treated with 0.3% hydrogen peroxide for 5 min, then rinsed in wash buffer, and incubated with 100 µg/mL salmon sperm and 5% FBS diluted in $1\times$ PBS for 15 min. Subsequently, cells were stained with 10 nM HJs for 1 h, washed, and incubated for 1 h with HRP-labeled streptavidin (DAKO, cat no. P039701-2) diluted 1:600 in $1\times$ PBS. Peroxidase activity was visualized by introducing DAB (DAKO, cat. no. K346711-2) as a substrate and incubated at RT until the resulting brown staining reached the desired intensity. Finally, cells were rinsed in wash buffer and counterstained with Mayer's Hematoxylin Solution (Abcam, cat. no. ab220365). A coverslip was mounted by adding an aqueous mounting medium (DAKO, cat. no. S302580-2). Immunostained cells were imaged on a Virtual Slide Scanner (Olympus VS120, Tokyo, Japan), using a bright-field microscope with a $20\times$ objective lens. The images were processed by using the software QuPath 0.4.3.

Immunogenicity studies

PBMCs were isolated from fresh heparinized blood obtained from a healthy donor by density gradient centrifugation using Ficoll-Paque Plus (GE Healthcare). The blood was diluted 1:1 with 0.9% NaCl and layered over the Ficoll-Paque gradient. After centrifugation at $400 \times g$ for 25 min at RT, the PBMC layer was carefully collected, washed twice with $1\times$ PBS supplemented with 0.5% BSA, and cryopreserved in FBS + 10% DMSO by slow freeze. For experimental analyses, cryopreserved samples were thawed in RPMI-1640 supplemented with glutamine, 10% FBS, 100 U/mL penicillin, and 100 µg/mL streptomycin. PBMCs were seeded in 48-well plates at a density of 5×10^5 cells per well in 300 µL complete RPMI-1640 medium. The cells were stimulated with HJs at a final concentration of 500 nM. As negative control, PBMCs were incubated only with medium while, for the positive control, cells were treated with 5 µg/mL LPS for 24 h and 5 mM ionomycin for 2 h. After 24 h incubation at $37^{\circ}C$ in a humidified atmosphere with 5% CO_2, the supernatants were collected by centrifugation at $200 \times g$ for 5 min, aliquoted, and stored at $-80^{\circ}C$. The concentrations of IFN-γ and TNF-α released in the supernatant were quantified using

commercially available enzyme-linked immunosorbent assay kits (TNF-α BMS223-4 and INF-γ BMS228, Invitrogen, CA) according to the manufacturer's instructions. In brief, 100 μL of standard solutions or 50 μL of supernatant were added in duplicates to the wells of a microtiter plate pre-coated with the respective capture antibody. Subsequently, 100 μL of biotin-conjugated detection antibody was added to each well and the plates were incubated for 2 h at RT. Following three washing steps, 100 μL of streptavidin-HRP was added and incubated for 1 h at RT. The plates were washed again, and 100 μL of tetramethyl-benzidine substrate solution was added to each well. The enzymatic reaction was stopped by adding 100 μL of 1 M phosphoric acid. The absorbance was measured at 450 nm using a microplate reader (CLARIOstar, BMG LABTECH, Germany). The concentrations of IFN-γ and TNF-α were calculated against standard curves created by using recombinant cytokine standards provided in the kits.

Animal model

Athymic nude female mice (6 weeks old) were purchased from Charles River and subcutaneously injected in the right hind leg with 10×10^6 SKOV3 cells in $1\times$ PBS. Tumors were allowed to grow for 5–8 weeks to reach 100–300 mm^3. The size of tumors was measured using a caliper and estimated using the formula (width $\times$ (length2))/2. The animal study protocol was approved by the ethical committee for animal research of the Vrije Universiteit Brussel (approval no. 20-272-18; license: LA1230272).

In vivo tumor targeting

The buffer-exchanged ^{67}Ga-labeled HJs in $1\times$ PBS (injection buffer) were filtered by using 0.22 μm syringe filters. Animals were randomized and distributed in six groups (three mice/group) for i.v. injection of the radiolabeled Nb and nanostructures. Xenografted mice administered with ^{99m}Tc-labeled 2Rs15d Nb were injected with a total of 0.9 nmol corresponding to 41.192 ± 0.178 MBq. Xenografted mice were administered with HJ-1x2Rs15d, HJ-2x2Rs15d, and HJ-2Rs15d-2Rb17c, and were respectively injected with 0.86 ± 0.03 nmol of construct, corresponding to 13.3 ± 0.4 MBq of radioactivity. Xenografted mice subjected to the negative control HJ constructs HJ-1xR3B23 and HJ-2xR3B23 were injected with 0.87 ± 0.09 nmol, corresponding to 11.6 ± 0.9 MBq of radioactivity. The accumulation of the radiolabeled tracers was evaluated *in vivo* by SPECT-CT imaging (MILabs) performed 1 h post-injection (p.i.), and *ex vivo* 1.5 h p.i., by isolating, weighing, and scanning organs and tissues by a γ-counter using standard samples of known activity as reference. The accumulated radioactivity recorded in tissues and organs was corrected for decay and expressed as %IA/g.

Statistical analysis

All statistical analyses were performed in GraphPad Prism 10 software (GraphPad, San Diego, CA). Results were expressed as mean ± SD. The specific statistical method employed and the number of replicates are indicated in the figure legends.

AUTHOR CONTRIBUTIONS

L.T. performed *in vitro* experiments and *in vivo* studies, data analysis, and manuscript writing with contributions from authors M.O., V.L.A., J.B., and J.K. S.K.O. performed the ICC experiment and the immunogenicity assessment. M.O. contributed to *in vitro* experiments, performed data analysis, and curated the graphic section of the manuscript. V.L.A. performed gel analysis of the constructs, and flow cytometry experiments, and contributed to the design and conceptualization of the studies. P.B. and J.S. contributed to *in vitro* experiments and fabricated the Nb-Q components of the HJ nanostructures. J.B. contributed to *in vitro* experiments, data analysis, and to the design and conceptualization of *in vivo* studies. J.S.N. performed preliminary *in vitro* experiments and contributed to the design and conceptualization of the studies. M.B.B. synthesized the reagent for Nb modification. S.H. contributed to the design and conceptualization of *in vivo* studies. K.V.G. contributed to securing the funding. J.K. conceptualized the study and secured the funding.

DECLARATION OF INTERESTS

The authors declare no competing interests.

SUPPLEMENTAL INFORMATION

Supplemental information can be found online at https://doi.org/10.1016/j.omtn.2024.102305.

REFERENCES

1. Sellmyer, M.A., Lee, I.K., and Mankoff, D.A. (2021). Building the Bridge: Molecular Imaging Biomarkers for 21st Century Cancer Therapies. J. Nucl. Med. *62*, 1672–1676. https://doi.org/10.2967/jnumed.121.262484.

2. Eckelman, W.C., Reba, R.C., and Kelloff, G.J. (2008). Targeted imaging: an important biomarker for understanding disease progression in the era of personalized medicine. Drug Discov. Today *13*, 748–759. https://doi.org/10.1016/j.drudis.2008.05.009.

3. Böhmer, V.I., Szymanski, W., Feringa, B.L., and Elsinga, P.H. (2021). Multivalent Probes in Molecular Imaging: Reality or Future? Trends Mol. Med. *27*, 379–393. https://doi.org/10.1016/j.molmed.2020.12.006.

4. Joshi, B.P., and Wang, T.D. (2010). Exogenous molecular probes for targeted imaging in Cancer: Focus on multi-modal imaging. Cancers *2*, 1251–1287. https://doi.org/10.3390/cancers2021251.

5. Lu, R.M., Hwang, Y.C., Liu, I.J., Lee, C.C., Tsai, H.Z., Li, H.J., and Wu, H.C. (2020). Development of therapeutic antibodies for the treatment of diseases. J. Biomed. Sci. *27*, 1–30. https://doi.org/10.1186/s12929-019-0592-z.

6. von Arx, C., De Placido, P., Caltavituro, A., Di Rienzo, R., Buonaiuto, R., De Laurentiis, M., Arpino, G., Puglisi, F., Giuliano, M., and Del Mastro, L. (2023). The evolving therapeutic landscape of trastuzumab-drug conjugates: Future perspectives beyond HER2-positive breast cancer. Cancer Treat Rev. *113*, 102500. https://doi.org/10.1016/j.ctrv.2022.102500.

7. Altunay, B., Morgenroth, A., Beheshti, M., Vogg, A., Wong, N.C.L., Ting, H.H., Biersack, H.J., Stickeler, E., and Mottaghy, F.M. (2021). HER2-directed antibodies, affibodies and nanobodies as drug-delivery vehicles in breast cancer with a specific focus on radioimmunotherapy and radioimmunoimaging. Eur. J. Nucl. Med. Mol. Imaging 48, 1371–1389. https://doi.org/10.1007/s00259-020-05094-1.

8. England, C.G., Ehlerding, E.B., Hernandez, R., Rekoske, B.T., Graves, S.A., Sun, H., Liu, G., McNeel, D.G., Barnhart, T.E., and Cai, W. (2017). Preclinical pharmacokinetics and biodistribution studies of 89Zr-Labeled Pembrolizumab. J. Nucl. Med. 58, 162–168. https://doi.org/10.2967/jnumed.116.177857.

9. Dammes, N., and Peer, D. (2020). Monoclonal antibody-based molecular imaging strategies and theranostic opportunities. Theranostics 10, 938–955. https://doi.org/10.7150/thno.37443.

10. Debie, P., Devoogdt, N., and Hernot, S. (2019). Targeted Nanobody-Based Molecular Tracers for Nuclear Imaging and Image-Guided Surgery. Antibodies 8, 12. https://doi.org/10.3390/ANTIB8010012.

11. Muyldermans, S. (2021). Applications of Nanobodies. Annu. Rev. Anim. Biosci. 9, 401–421. https://doi.org/10.1146/annurev-animal-021419-083831.

12. Bao, G., Tang, M., Zhao, J., and Zhu, X.N. (2021). a promising toolkit for molecular imaging and disease therapy. EJNMMI Res. 11, 1–13. https://doi.org/10.1186/s13550-021-00750-5.

13. Xenaki, K.T., Oliveira, S., and van Bergen en Henegouwen, P.M.P. (2017). Antibody or antibody fragments: Implications for molecular imaging and targeted therapy of solid tumors. Front. Immunol. 8, 1287. https://doi.org/10.3389/fimmu.2017.01287.

14. Bates, A., and Power, C.A. (2019). Goliath: The Structure, Function, and Clinical Prospects of Antibody Fragments. Antibodies 8, 28. https://doi.org/10.3390/ANTIB8020028.

15. Xavier, C., Vaneycken, I., D'huyvetter, M., Heemskerk, J., Keyaerts, M., Vincke, C., Devoogdt, N., Muyldermans, S., Lahoutte, T., and Caveliers, V. (2013). Synthesis, preclinical validation, dosimetry, and toxicity of 68Ga-NOTA-anti-HER2 nanobodies for iPET imaging of HER2 receptor expression in cancer. J. Nucl. Med. 54, 776–784. https://doi.org/10.2967/jnumed.112.111021.

16. Chigoho, D.M., Lecocq, Q., Awad, R.M., Breckpot, K., Devoogdt, N., Keyaerts, M., Caveliers, V., Xavier, C., and Bridoux, J. (2021). Site-specific radiolabeling of a human pd-l1 nanobody via maleimide–cysteine chemistry. Pharmaceuticals 14, 550. https://doi.org/10.3390/ph14060550.

17. Renard, E., Collado Camps, E., Canovas, C., Kip, A., Gotthardt, M., Rijpkema, M., Denat, F., Goncalves, V., and van Lith, S.A.M. (2021). Site-specific dual-labeling of a vhh with a chelator and a photosensitizer for nuclear imaging and targeted photodynamic therapy of egfr-positive tumors. Cancers 13, 428–515. https://doi.org/10.3390/cancers13030428.

18. Bridoux, J., Broos, K., Lecocq, Q., Debie, P., Martin, C., Ballet, S., Raes, G., Neyt, S., Vanhove, C., Breckpot, K., et al. (2020). Anti-human pd-l1 nanobody for immunopet imaging: Validation of a conjugation strategy for clinical translation. Biomolecules 10, 1388–1415. https://doi.org/10.3390/biom10101388.

19. Massa, S., Vikani, N., Betti, C., Ballet, S., Vanderhaegen, S., Steyaert, J., Descamps, B., Vanhove, C., Bunschoten, A., van Leeuwen, F.W.B., et al. (2016). Sortase A-mediated site-specific labeling of camelid single-domain antibody-fragments: a versatile strategy for multiple molecular imaging modalities. Contrast Media Mol. Imaging 11, 328–339. https://doi.org/10.1002/cmmi.1696.

20. Teodori, L., Omer, M., Märcher, A., Skaanning, M.K., Andersen, V.L., Nielsen, J.S., Oldenburg, E., Lin, Y., Gothelf, K.V., and Kjems, J. (2022). Site-specific nanobody-oligonucleotide conjugation for super-resolution imaging. J. Biol. Methods 9, e159. https://doi.org/10.14440/jbm.2022.381.

21. Bannas, P., Lenz, A., Kunick, V., Well, L., Fumey, W., Rissiek, B., Haag, F., Schmid, J., Schütze, K., Eichhoff, A., et al. (2015). Molecular imaging of tumors with nanobodies and antibodies: Timing and dosage are crucial factors for improved in vivo detection. Contrast Media Mol. Imaging 10, 367–378. https://doi.org/10.1002/cmmi.1637.

22. Debie, P., Lafont, C., Defrise, M., Hansen, I., van Willigen, D.M., van Leeuwen, F.W.B., Gijsbers, R., D'Huyvetter, M., Devoogdt, N., Lahoutte, T., et al. (2020). Size and affinity kinetics of nanobodies influence targeting and penetration of solid tumours. J. Control. Release 317, 34–42. https://doi.org/10.1016/j.jconrel.2019.11.014.

23. Hu, Y., Liu, C., and Muyldermans, S. (2017). Nanobody-based delivery systems for diagnosis and targeted tumor therapy. Front. Immunol. 8, 1442. https://doi.org/10.3389/fimmu.2017.01442.

24. Tijink, B.M., Laeremans, T., Budde, M., Stigter-van Walsum, M., Dreier, T., de Haard, H.J., Leemans, C.R., and van Dongen, G.A.M.S. (2008). Improved tumor targeting of anti-epidermal growth factor receptor Nanobodies through albumin binding: Taking advantage of modular Nanobody technology. Mol. Cancer Ther. 7, 2288–2297. https://doi.org/10.1158/1535-7163.MCT-07-2384.

25. Albert, S., Arndt, C., Koristka, S., Berndt, N., Bergmann, R., Feldmann, A., Schmitz, M., Pietzsch, J., Steinbach, J., and Bachmann, M. (2018). From mono- to bivalent: Improving theranostic properties of target modules for redirection of UniCAR T cells against EGFR-expressing tumor cells in vitro and in vivo. Oncotarget 9, 25597–25616. https://doi.org/10.18632/oncotarget.25390.

26. Sadeghi, A., Behdani, M., Muyldermans, S., Habibi-Anbouhi, M., and Kazemi-Lomedasht, F. (2020). Development of a mono-specific anti-VEGF bivalent nanobody with extended plasma half-life for treatment of pathologic neovascularization. Drug Test. Anal. 12, 92–100. https://doi.org/10.1002/dta.2693.

27. Moliner-morro, A., Sheward, D., Karl, V., Perez Vidakovics, L., Murrell, B., McInerney, G.M., and Hanke, L. (2020). Picomolar sars-cov-2 neutralization using multi-arm peg nanobody constructs. Biomolecules 10, 1–11. https://doi.org/10.3390/biom10121661.

28. Iqbal, U., Trojahn, U., Albaghdadi, H., Zhang, J., O'Connor-McCourt, M., Stanimirovic, D., Tomanek, B., Sutherland, G., and Abulrob, A. (2010). Kinetic analysis of novel mono- and multivalent VHH-fragments and their application for molecular imaging of brain tumours: RESEARCH PAPER. Br. J. Pharmacol. 160, 1016–1028. https://doi.org/10.1111/j.1476-5381.2010.00742.x.

29. Wang, Y., Wang, Y., Chen, G., Li, Y., Xu, W., and Gong, S. (2017). Quantum-Dot-Based Theranostic Micelles Conjugated with an Anti-EGFR Nanobody for Triple-Negative Breast Cancer Therapy. ACS Appl. Mater. Interfaces 9, 30297–30305. https://doi.org/10.1021/acsami.7b05654.

30. D'Hollander, A., Jans, H., Velde, G.V., Verstraete, C., Massa, S., Devoogdt, N., Stakenborg, T., Muyldermans, S., Lagae, L., and Himmelreich, U. (2017). Limiting the protein corona: A successful strategy for in vivo active targeting of anti-HER2 nanobody-functionalized nanostars. Biomaterials 123, 15–23. https://doi.org/10.1016/j.biomaterials.2017.01.007.

31. Yu, Z., Hu, M., Li, Z., Dan Xu, Zhu, L., Guo, Y., Liu, Q., Lan, W., Jiang, J., and Wang, L. (2020). Anti-G250 nanobody-functionalized nanobubbles targeting renal cell carcinoma cells for ultrasound molecular imaging. Nanotechnology 31, 205101. https://doi.org/10.1088/1361-6528/ab7040.

32. Punjabi, M., Xu, L., Ochoa-Espinosa, A., Kosareva, A., Wolff, T., Murtaja, A., Broisat, A., Devoogdt, N., and Kaufmann, B.A. (2019). Ultrasound Molecular Imaging of Atherosclerosis with Nanobodies: Translatable Microbubble Targeting Murine and Human VCAM (Vascular Cell Adhesion Molecule) 1. Arterioscler. Thromb. Vasc. Biol. 39, 2520–2530. https://doi.org/10.1161/ATVBAHA.119.313088.

33. Bannas, P., Hambach, J., and Koch-Nolte, F. (2017). Nanobodies and nanobody-based human heavy chain antibodies as antitumor therapeutics. Front. Immunol. 8, 1603. https://doi.org/10.3389/fimmu.2017.01603.

34. Kolkman, J.A., and Law, D.A. (2010). Nanobodies - From llamas to therapeutic proteins. Drug Discov. Today Technol. 7, e139–e146. https://doi.org/10.1016/j.ddtec.2010.03.002.

35. Wang, J., Kang, G., Yuan, H., Cao, X., Huang, H., and de Marco, A. (2021). Research Progress and Applications of Multivalent, Multispecific and Modified Nanobodies for Disease Treatment. Front. Immunol. 12, 838082. https://doi.org/10.3389/fimmu.2021.838082.

36. Jonasson, P., Liljeqvist, S., Nygren, P.-Å., and Ståhl, S. (2002). Genetic design for facilitated production and recovery of recombinant proteins in Escherichia coli. Biotechnol. Appl. Biochem. 35, 91–105. https://doi.org/10.1042/ba20010099.

37. Vaneycken, I., Devoogdt, N., Van Gassen, N., Vincke, C., Xavier, C., Wernery, U., Muyldermans, S., Lahoutte, T., and Caveliers, V. (2011). Preclinical screening of anti-HER2 nanobodies for molecular imaging of breast cancer. Faseb. J. 25, 2433–2446. https://doi.org/10.1096/fj.10-180331.

38. D'Huyvetter, M., De Vos, J., Xavier, C., Pruszynski, M., Sterckx, Y.G.J., Massa, S., Raes, G., Caveliers, V., Zalutsky, M.R., Lahoutte, T., and Devoogdt, N. (2017).

131I-labeled anti-HER2 camelid sdAb as a theranostic tool in cancer treatment. Clin. Cancer Res. *23*, 6616–6628. https://doi.org/10.1158/1078-0432.CCR-17-0310.

39. Andersen, V.L., Vinther, M., Kumar, R., Ries, A., Wengel, J., Nielsen, J.S., and Kjems, J. (2019). A self-assembled, modular nucleic acid-based nanoscaffold for multivalent theranostic medicine. Theranostics *9*, 2662–2677. https://doi.org/10.7150/thno.32060.

40. Omer, M., Andersen, V.L., Nielsen, J.S., Wengel, J., and Kjems, J. (2020). Improved Cancer Targeting by Multimerizing Aptamers on Nanoscaffolds. Mol. Ther. Nucleic Acids *22*, 994–1003. https://doi.org/10.1016/j.omtn.2020.10.013.

41. Lemaire, M., D'Huyvetter, M., Lahoutte, T., Van Valckenborgh, E., Menu, E., De Bruyne, E., Kronenberger, P., Wernery, U., Muyldermans, S., Devoogdt, N., and Vanderkerken, K. (2014). Imaging and radioimmunotherapy of multiple myeloma with anti-idiotypic Nanobodies. Leukemia *28*, 444–447. https://doi.org/10.1038/leu.2013.292.

42. Mota, A.d.L., Evangelista, A.F., Macedo, T., Oliveira, R., Scapulatempo-Neto, C., Vieira, R.A., and Marques, M.M.C. (2017). Molecular characterization of breast cancer cell lines by clinical immunohistochemical markers. Oncol. Lett. *13*, 4708–4712. https://doi.org/10.3892/ol.2017.6093.

43. Ramadan, W.S., Vazhappilly, C.G., Saleh, E.M., Menon, V., AlAzawi, A.M., El-Serafi, A.T., Mansour, W., and El-Awady, R. (2018). Interplay between epigenetics, expression of estrogen receptor- α, HER2/ERBB2 and sensitivity of triple negative breast cancer cells to hormonal therapy. Cancers *11*, 13. https://doi.org/10.3390/cancers11010013.

44. Yu, X., Ghamande, S., Liu, H., Xue, L., Zhao, S., Tan, W., Zhao, L., Tang, S.C., Wu, D., Korkaya, H., et al. (2018). Targeting EGFR/HER2/HER3 with a Three-in-One Aptamer-siRNA Chimera Confers Superior Activity against HER2+ Breast Cancer. Mol. Ther. Nucleic Acids *10*, 317–330. https://doi.org/10.1016/J.OMTN.2017.12.015.

45. Subik, K., Lee, J.F., Baxter, L., Strzepek, T., Costello, D., Crowley, P., Xing, L., Hung, M.C., Bonfiglio, T., Hicks, D.G., and Tang, P. (2010). The expression patterns of ER, PR, HER2, CK5/6, EGFR, KI-67 and AR by immunohistochemical analysis in breast cancer cell lines. Breast Cancer *4*, 35–41. https://doi.org/10.1177/117822341000400004.

46. Moghimi, S.M. (1995). Mechanisms of splenic clearance of blood cells and particles: towards development of new splenotropic agents. Adv. Drug Deliv. Rev. *17*, 103–115. https://doi.org/10.1016/0169-409X(95)00043-7.

47. Wang, B., He, X., Zhang, Z., Zhao, Y., and Feng, W. (2013). Metabolism of Nanomaterials in Vivo: Blood Circulation and Organ Clearance. Acc. Chem. Res. *46*, 761–769. https://doi.org/10.1021/ar2003336.

48. Haute, D.V., and Berlin, J.M. (2017). Challenges in realizing selectivity for nanoparticle biodistribution and clearance: Lessons from gold nanoparticles. Ther. Deliv. *8*, 763–774. https://doi.org/10.4155/tde-2017-0057.

49. Cheng, P., and Pu, K. (2021). Molecular imaging and disease theranostics with renal-clearable optical agents. Nat. Rev. Mater. *6*, 1095–1113. https://doi.org/10.1038/s41578-021-00328-6.

50. Tsoi, K.M., MacParland, S.A., Ma, X.Z., Spetzler, V.N., Echeverri, J., Ouyang, B., Fadel, S.M., Sykes, E.A., Goldaracena, N., Kaths, J.M., et al. (2016). Mechanism of hard-nanomaterial clearance by the liver. Nat. Mater. *15*, 1212–1221. https://doi.org/10.1038/nmat4718.

51. Gustafson, H.H., Holt-Casper, D., Grainger, D.W., and Ghandehari, H. (2015). Nanoparticle uptake: The phagocyte problem. Nano Today *10*, 487–510. https://doi.org/10.1016/j.nantod.2015.06.006.

52. Yadav, D., and Dewangan, H.K. (2021). PEGYLATION: an important approach for novel drug delivery system. J. Biomater. Sci. Polym. Ed. *32*, 266–280. https://doi.org/10.1080/09205063.2020.1825304.

53. Shi, D., Beasock, D., Fessler, A., Szebeni, J., Ljubimova, J.Y., Afonin, K.A., and Dobrovolskaia, M.A. (2022). To PEGylate or not to PEGylate: Immunological properties of nanomedicine's most popular component, polyethylene glycol and its alternatives. Adv. Drug Deliv. Rev. *180*, 114079. https://doi.org/10.1016/j.addr.2021.114079.

54. Ibrahim, M., Ramadan, E., Elsadek, N.E., Emam, S.E., Shimizu, T., Ando, H., Ishima, Y., Elgarhy, O.H., Sarhan, H.A., Hussein, A.K., and Ishida, T. (2022). Polyethylene glycol (PEG): The nature, immunogenicity, and role in the hypersensitivity of PEGylated products. J. Control. Release *351*, 215–230. https://doi.org/10.1016/j.conrel.2022.09.031.

55. Bienk, K., Hvam, M.L., Pakula, M.M., Dagnæs-Hansen, F., Wengel, J., Malle, B.M., Kragh-Hansen, U., Cameron, J., Bukrinski, J.T., and Howard, K.A. (2016). An albumin-mediated cholesterol design-based strategy for tuning siRNA pharmacokinetics and gene silencing. J. Control. Release *232*, 143–151. https://doi.org/10.1016/j.jconrel.2016.04.013.

56. Swain, S.M., Shastry, M., and Hamilton, E. (2023). Targeting HER2-positive breast cancer: advances and future directions. Nat. Rev. Drug Discov. *22*, 101–126. https://doi.org/10.1038/s41573-022-00579-0.

57. Zhou, L., Yang, F., Bai, Z., Zhou, X., Zhang, Z., Li, Z., Gong, J., Yu, J., Pan, L., Cao, C., and Chou, J.J. (2023). Self-Assembled L–DNA Linkers for Rapid Construction of Multi-Specific Antibody-Drug Conjugates Library. Angew. Chem. Int. Ed. Engl. *62*, e202302805. https://doi.org/10.1002/anie.202302805.

58. Ščasnár, V., and van Lier, J.E. (1993). The use of SEP-PAK Sl cartridges for the preparation of gallium chloride from the citrate solution. Eur. J. Nucl. Med. *20*, 273. https://doi.org/10.1007/BF00170012.